Atmos. Chem. Phys. Discuss., 5, 9547–9580, 2005
www.atmos-chem-phys.org/acpd/5/9547/
SRef-ID: 1680-7375/acpd/2005-5-9547
European Geosciences Union

Atmospheric
Chemistry
and Physics
Discussions

Liquid particle composition and heterogeneous reactions in a mountain wave Polar Stratospheric Cloud

D. Lowe[1], A. R. MacKenzie[1], H. Schlager[2], C. Voigt[2], A. Dörnbrack[2], M. J. Mahoney[3], and F. Cairo[4]

[1]Environmental Science Dept., Lancaster University, Lancaster, UK
[2]Institute for Atmospheric Physics, DLR, Oberpfaffenhofen, Germany
[3]Jet Propulsion Laboratory, California Institute of Technology, Pasadena, California, USA
[4]Institute of Atmospheric Sciences and Climate of the National Research Council (CNR-ISAC), Rome, Italy

Received: 25 April 2005 – Accepted: 1 July 2005 – Published: 4 October 2005

Correspondence to: A. R. MacKenzie (r.mackenzie@lancaster.ac.uk)

Abstract

Mountain wave polar stratospheric clouds (PSCs) were detected on 8 February 2003 above the Scandinavian Mountains by in-situ instruments onboard the M55 Geophysica aircraft. The observations of PSC particle composition, backscatter and chlorine activation are studied with a recently developed dynamical microphysical non-equilibrium box model. Results from the microphysical model, run on quasi-lagrangian trajectories, show that the PSC is composed of supercooled ternary ($H_2O/HNO_3/H_2SO_4$) solutions (STS) particles, which are out of equilibrium with the gas phase. The optical properties of the PSC can well be simulated with the model. Up to 0.15 ppbv Cl_2 can be released by the PSC within 2 h in reasonable agreement with the measured ClO_x concentrations, but high solar zenith angles prevent a direct comparison. Equilibrium calculations commonly used in large scale chemistry transport models poorly represent the measured PSC particle composition and chlorine activation under mountain wave conditions.

1. Introduction

Polar stratospheric clouds (PSCs) have long been recognised to play an important role in the destruction of stratospheric ozone via chlorine activation, dehydration and denitrification (for a detailed review and discussion see, for example, WMO, 2003, and references within). PSCs are, however, composed of a range of different particles, both solid and liquid, the combination of which governs their environmental influence. Below the frost point solid type II particles can exist, composed of water ice. Up to several degrees above the frost point HNO_3-rich type I particles can form. These can consist of solid nitric acid trihydrate (NAT) (Hanson and Mauersberger, 1988) as observed by balloon-borne in-situ mass spectrometry (Voigt et al., 2000a) – or possibly dihydrate (NAD) (Worsnop et al., 1993). Additionally, supercooled ternary solution (STS) droplets (Molina et al., 1993; Zhang et al., 1993; Carslaw et al., 1994) form 3–4 K above the ice frostpoint.

The heterogeneous chemical processes involved in chlorine activation have been extensively studied in laboratory work (see, for example, Sander et al., 2003, and references within. A notable omission in these studies is noted in Section 4.1, however.). Whilst the majority of the chemical constituents involved in these processes have been measured on a range of scales, from in-situ to global, modelling studies of chlorine activation have tended to focus on global/mesoscale effects, originally incorporating the heterogeneous processes as empirical effects, which are compared with large-scale rather than in-situ observations (e.g. Kühl et al., 2004). Recent work has incorporated microphysical PSC schemes into mesoscale chemical models (Drdla and Schoeberl, 2003; Mann et al., 2003). Microphysical models have previously been used to model chlorine activation, initially considering just background aerosols and NAT PSCs (Jones et al., 1990; Lutman et al., 1994), but later considering more complicated populations of particles (Drdla, 1996; Sessler et al., 1996; Carslaw et al., 1998). However these models have never been compared with measurements of chlorine within PSCs, mainly because most measurements of PSCs have been remote rather than in-situ.

Until recently the chemical compositions of PSC particles have had to be inferred from gas-phase compositions and the polarisation of lidar signals; however this has been changed by the development of balloon-borne mass spectrometers (Schreiner et al., 1999), and aeroplane-borne chemiluminescence instruments (Northway et al., 2002), designed to measure the NO_y content of the particle phase.

These balloon-borne in-situ measurements positively identified NAT (Voigt et al., 2000a) and STS (Voigt et al., 2000b) in mountain wave PSCs. More recently such measurements have also been used to confirm the presence on HCl in STS particles (Weisser et al., 2004). Because the balloons carrying these instruments follow quasi-lagrangian flight-paths the measurements are highly suited to the creation of lagrangian trajectories for 0-D models (Voigt et al., 2003). In addition, in-situ measurements of the NO_y content of the particle and gas phases allowed the identification of very low number densities of relatively large (5 µm radius) NAT particles (so-called “NAT-rocks”) during the SOLVE/THESEO 2000 campaign (Fahey et al., 2001).

The microphysical studies mentioned above concentrated purely on particle compositions, with no consideration of the heterogeneous reactions occurring on these particles. Studies of these reactions which use a microphysical box-model (e.g. Carslaw et al., 1998) have not been able to make comparisons of the model output with in-situ measurements of the changes in the mixing ratios of chlorine compounds passing through the PSC event. One of the aims of the VINTERSOL-EuPLEx campaign is to study halogen activation within PSCs. To this end the M-55 Geophysica aircraft was fitted with instruments to make in-situ measurements of particle composition and a number of chlorine species. Care was taken to fly the Geophysica parallel to the wind-direction close to, or within, PSCs in order to allow quasi-lagrangian studies of the evolution of these PSC properties to be made. Below we will examine one such flight from EuPLEx, comparing the particle compositions with those calculated by our microphysical model (Lowe et al., 2003), and with an equilibrium composition STS model such as commonly used in chemistry-transport models (e.g. Sessler et al., 1996). We shall examine the differences in Cl_2 production between the two models, and qualitatively compare their output to the measured mixing ratios of ClO_x.

2. Meteorological forecast and flight plan

The meteorological conditions above northern Scandinavia on 8 February 2003 were favourable for the excitation and vertical propagation of mountain waves. These waves formed mesoscale stratospheric temperature anomalies which extended from directly above to around 200 km downstream of the mountain range (Fig. 1). The hindcast simulation from the MM5 mesoscale model indicates the presence of two nearly parallel regions of low temperatures with a peak-to-peak amplitude of about 12 K, whereas the cooling with respect to the upstream conditions amounts to about 6 K.

Tropospheric excitation conditions varied on 8 February 2003, so that the stratospheric mountain wave event only lasted for about 6 h. Therefore, and in contrast to former documented events (Dörnbrack et al., 1999, 2002), the cooling within the waves was limited to 6 K.

Based on the MM5 forecasts (Dörnbrack et al., 1998) a flight plan was drawn up for the Geophysica to include several passes through these mountain waves parallel to the wind direction; on the day the flight path was fine-tuned using lidar observations from the Falcon aircraft. The Geophysica passed through a number of PSCs, the positions of which are indicated in Fig. 2.

3. Measurements

The Geophysica aircraft carries a wide-range of instruments, from lidar through to whole-air samplers (Stefanutti et al., 2004); in this study, however, we shall primarily use data from the SIOUX instrument (Schmitt, 2003; Voigt et al., 2005) – a chemiluminescence detector similar to that used by Northway et al. (2002) on the ER-2 aircraft. We will also use temperature data from the JPL MTP (Microwave Temperature Profiler) instrument (Denning et al., 1989); aerosol backscatter data from the MAS instrument (Adriani et al., 1999); total H_2O mixing ratios from the FISH (Fast In-Situ Hygrometer (Zöger et al., 1999); N_2O mixing ratios from the HAGAR instrument (Stefanutti et al., 2004); and ClO, ClOOCl and $ClONO_2$ mixing ratios from the HALOX (HALogen OXide monitor) instrument (Brune et al., 1989; von Hobe et al., 2005). Although the Geophysica carried a FSSP aerosol spectrometer to measure the aerosol size distribution, it was not operational during the part of the flight discussed below.

The SIOUX instrument (Schmitt, 2003; Voigt et al., 2005) located in the right wing pod of the aircraft M55 Geophysica has two inlets, which are especially designed for PSC measurements. Particle- and gas-phase NO_y (total NO_y) are detected using a forward facing inlet. The measured particle number density is enhanced due to anisokinetic sampling of the particles, the enhancement factor is dependent on pressure and particle size. The rear facing inlet primarily measures the gas phase; particles with diameters >0.2 µm are excluded due to inertia. Inside the inlets the particles evaporate, NO_y is catalytically reduced to NO, and the subsequent reaction of NO with ozone is measured with a chemiluminiscence detector. Nitric acid content of the particles is derived by subtracting the gas phase NO_y from the total NO_y and correcting for the particle enhancement. In this work, we use an oversampling factor of 3.6 for particles smaller than 0.3 µm at pressures near 50 mbar, derived from inlet simulations (Krämer and Afchine, 2004). The oversampling factor increases for larger particles and decreases for lower pressures.

Measurements taken by the SIOUX instrument during this flight are shown in Fig. 3. The discrepancies between the total (red line) and gas-phase (black line) NO_y occur when particles are present. We shall concentrate on the second, Northern, PSC event: denoted by the green lines in Figs. 2 and 3. The section of the flight that passes through this PSC was in the direction of, and practically parallel to, the local wind; this allows us to use the flight to construct a quasi-lagrangian trajectory. We will not use the earlier PSC event (denoted by the blue line in Fig. 2) for a case study. This is done because the magnitudes of the MAS and SIOUX data within this event are not as great as those of the later event, to the degree that the signal in the SIOUX data is below the instruments detection limit. Additionally the Geophysicas flight path is not parallel to the wind direction throughout all of the earlier PSC observations, and so is not suitable use within quasi-lagrangian trajectories.

The MAS instrument (Adriani et al., 1999) is a short range lidar instrument which measures aerosol backscatter. Measurements cover a volume of air some 2–30 m in front of the aircraft, with a peak signal at 3–5 m from the aircraft (which we will use for this work). Because of this the instrument is a close-range remote sensor rather than an in-situ sensor, however the range of the instrument is short enough that we can compare the results with in-situ measurements. The MAS instrument uses the wavelengths 532 nm and 1064 nm, however the 1064 nm data was very noisy during this flight, so we will just use the 532 nm data. Measurements taken by the MAS instrument are shown in Fig. 4. This shows an increase in backscatter within the mountain-wave event, indicating an increase in the mass of the aerosol phase.

To create trajectories for our model we shall use temperature and pressure measurements made during the flight. In-situ measurements of these were made by the Geophysica's navigational data system (UCSE) and the MTP instrument. Additionally the variations in temperature within 5 km of the flight path altitude can be reliably obtained using the MTP measurements – the estimated errors in temperature relative to radiosondes are ±0.5 K at flight level, less than ±1.0 K within 2.2 km of flight level, and less than ±2.0 K within 6 km of flight level. Using this data we compare the changes in the aircraft pressure altitude with those of the isentropic surfaces within the mountain wave (Fig. 5). Before the mountain wave the aircraft flies just above the 455 K isentrope, following its profile well. Within the mountain wave ($t \approx 18.27$–18.5 h), however, the aircraft drops about 10 K in potential temperature, before returning to roughly follow the 455 K isentrope again. These changes in potential temperature mean that the aircraft trajectory is not ideal for studying the evolution of the PSC particles; in the work below we will investigate this influence on our attempts to replicate the NO_y observations.

Comparisons of the UCSE data with measurements from the MTP show that, on average over the whole campaign, $T_{UCSE} = T_{MTP} - 1.14$ K. For the 8 February flight this difference becomes $T_{UCSE} = T_{MTP} - 1.63$ K. The MTP data are calibrated using measurements from radiosondes launched close to the flight path of the Geophysica and so are likely to be the most reliable temperature measurements; however the higher temporal resolution of the UCSE data is useful for our work, and so we will use this for our trajectories, although with corrections to bring the temperature in line with the MTP measurements.

4. Model details

We will use two box models to calculate the evolution of, and heterogeneous reactions on, the aerosol along a trajectory passing through the mountain wave. The first uses the parameterisation of Carslaw et al. (1995) to calculate the composition of STS in equilibrium with the gas-phase, from which we calculate the aerosol surface area for

Title Page
Abstract Introduction
Conclusions References
Tables Figures
◄ ►
Back Close
Full Screen / Esc
Print Version
Interactive Discussion

EGU

a prescribed particle number density. The second, MADVEC, describes the dynamics of condensational growth of liquid PSC particles, using the advection of mass components in radius-space (Pilinis, 1990) driven by differences between ambient partial pressures and the equilibrium vapour pressures parameterised by Luo et al. (1995). This scheme allows us to treat particle growth as the advection of mass in size-space using fluid dynamical methods (see Lowe et al., 2003, for more details).

4.1. Heterogeneous chemical reactions

To the box models we have added parameterisations of heterogeneous reactions for the release of Cl_2 and HOCl:

$$ClONO_2 + H_2O(l) \rightarrow HOCl + HNO_3(aq), \tag{R1}$$

$$ClONO_2 + HCl(aq) \rightarrow Cl_2 + HNO_3(aq), \tag{R2}$$

$$HOCl + HCl(aq) \rightarrow Cl_2 + H_2O(l). \tag{R3}$$

No gas-phase homogeneous reactions have yet been incorporated into the box models; so we do not currently model the photolytic conversion of Cl_2 into ClO, or the re-combination of ClO and NO_2 to form $ClONO_2$. The first of these processes would not be relevant for these test-cases due to the high solar zenith angles. The second process could slightly increase the yield of ClO_x and HOCl from Reactions (R1) and (R2) since HCl is initialised in excess of $ClONO_2$ (see Sect. 5.2); therefore the yields reported below are lower limits.

There are no parameterisations for the rates of Reactions (R1)–(R3) on STS; instead we will use the parameterisations for binary sulphate solutions calculated by Shi et al. (2001). Their parameterisations are based on the water activity of the binary solution – which is dependent on the atmospheric conditions rather than the composition of the solution. To use their solution we simply insert the water activity of the STS droplets.

This method may, however, lead to an over estimation of the production rates of Cl_2 and HOCl during our test-cases. Hanson (1998) has compared measured uptake coefficients for Reactions (R1)–(R3) on ternary HNO_3/H_2SO_4 solutions with the calculated coefficients for binary sulphate solutions of the same water activity. He found that the uptake coefficients for ternary solutions were typically 30–50% less than would be expected for binary solutions with the same water activity. In addition we should note that the uptake coefficients given by the parameterisation of Shi et al. (2001) are, generally, greater than those used by Hanson (1998), which will increase any over-prediction in production rates (see Shi et al., 2001, Fig. 6, for comparison).

In both box-models we will treat $ClONO_2$, HOCl and HCl as purely gas-phase species; principally because the calculations of Shi et al. (2001) use the gas-phase concentration of HCl, and include terms to account for the depletion of HCl in the condensed-phase. However, because of the relatively small saturation ratios of HCl, this assumption of equilibrium is not unreasonable. Any gains or losses of H_2O or HNO_3 by reaction are applied to the condensed phase, however these are not large enough to make any significant difference to particle compositions.

5. Test case settings

5.1. Trajectories

Synoptic-scale back trajectories (based on ECMWF-analysis; http://badc.nerc.ac.uk/data/ecmwf-trj/) from the start of the second PSC event show that the temperature of the air-parcel was above 200 K for a period of at least 10–120 h before the mountain wave event (Fig. 6a). As such we can assume that any PSC particles observed within the mountain wave event are less than 10–15 h old.

We have used two methods to generate trajectories for our models. In the first we have combined a 6 h MM5 back-trajectory (Wernli and Davis, 1997) with adapted temperature and pressure measurements from the Geophysica aircraft (Fig. 6b). To account for the differences between the aircraft and wind speeds we have multiplied the timescale of the aircraft data by the ratio of the aircraft speed to wind speed at each data point. This increases the time taken by a factor of 7–8. To account for differences between UCSE and MTP (see Sect. 3), we add 1.5 K to T_{UCSE}. This produces a good fit to the magnitude of the MTP data (compare the green (T_{UCSE} + 1.5 K) and black (MTP) lines in Fig. 6b), allowing us to retain the higher temporal resolution of the UCSE data.

However, as discussed above (see Sect. 3), the trajectory followed by the aircraft within the gravity wave was not isentropic. To study what influence this will have on modelling the observations we will also use four isentropic trajectories – along the 445 K, 450 K, 455 K and 460 K surfaces (see Fig. 5) – derived from the MTP data.

It should be noted that, within the mountain wave, neither the MM5 model nor the ECMWF analysis predict temperatures as low as 192 K. Without temperatures lower than this the STS droplets will not grow very much, there would be little difference between the equilibrium and microphysical models, and so using these trajectories for model runs would not provide any extra information.

5.2. Model initialisation

We initialise our microphysical aerosol model with 4.8 ppmv H_2O, 8.1 ppbv HNO_3, 0.5 ppbv H_2SO_4, and a log-normal particle distribution with mode radius 0.067 µm, width 1.8, and number density of 10 cm^{-3}. The H_2O and HNO_3 mixing ratios are approximations taken, respectively, from FISH and SIOUX data during the second PSC event. The H_2SO_4 mixing ratio and particle number density are based on standard values for this part of the stratosphere. In the stratosphere reactive nitrogen (NO_y) is composed of NO, NO_2, NO_3, N_2O_5, HONO, HO_2NO_2, HNO_3, PAN, and $ClONO_2$. For this work, however, we will assume that all of the particulate NO_y is in the form of HNO_3.

To initialise the chlorine compounds within our model we will use the scheme of Schauffler et al. (2003), which is based on data collected during the SOLVE campaign in January–March 2000. Using this scheme we calculate the total inorganic chlorine based on the N_2O content of the air parcel (determined by HAGAR to be approximately 135 ppb within the second PSC event), then remove the measured amounts of ClO_x and $ClONO_2$ (from HALOX) to obtain an amount of HCl. Hence we calculate a total inorganic chlorine mixing ratio of 2800 ppt, 300 ppt ClO_x, 500 ppt $ClONO_2$ and 2000 ppt HCl. The ClO_x data are uncertain by 30%. Although the results are sensitive to these uncertainties, the relative magnitudes of the results are less so, and thus neither are our conclusions.

6. Results

6.1. Particle composition

In Fig. 7 the particle-phase NO_y content of our microphysical model (green, light blue and purple lines, as identified in the legend) is compared with that measured by the SIOUX instrument (black line). The SIOUX instrument does not distinguish particles with radii <0.1 µm from the gas phase (see Sect. 3), leading to an underestimation of the NO_y content of the condensed phase. To account for this when making comparisons between SIOUX and model data we will also not include the NO_y content of particles with radii <0.1 µm in the total condensed phase NO_y content. The effect of this is to reduce the HNO_3 content by 5–15%.

From Fig. 7 we see that the model runs along the 450 K, and 455 K isentropes, as well as that run along the 460 K isentrope (not shown), produce quite low particle-phase NO_y contents, whereas that produced by the 445 K model run is much higher – with a maximum of ≈0.5 ppbv NO_y in the particle-phase, comparable with the maxima of the SIOUX data, and ≤0.3 ppbv for the other model runs. The greater differences between the output from the 445 K and 450 K model runs, as opposed to, for example, the 450 K and 455 K runs, occur because these two trajectories straddle the narrow range of temperatures over which the liquid aerosol particles change composition from binary sulphate to ternary solutions.

Although the 445 K model run is the best at replicating the magnitude of the SIOUX measurements, it does not fully capture some of the rapid changes in NO_y content measured by the SIOUX instrument. As discussed above, these changes occur as the aircraft crosses isentropic levels, so sampling air-parcels with different temperature histories. To simulate this we have calculated the expected particle-phase NO_y content along the T_{UCSE} + 1.5 K trajectory by interpolating between the neighbouring two isentropic trajectories based on the calculated potential temperature for the T_{UCSE} + 1.5 K trajectory (where the trajectory passes outside of this range of potential temperatures, e.g. at time $t{\approx}0.9$ h, we simply use the value for the nearest isentropic trajectory). The result is shown by the red line in Fig. 7a, and it retains the maximum NO_y content of approximately 0.5 ppbv of the 445 K model run, although for the majority of the mountain wave event the NO_y content is closer to the 450 K model run.

In Fig. 8a we compare the resulting particle-phase NO_y content from the combination of the isentropic trajectories with that resulting from simply running our microphysical model along the T_{UCSE} + 1.5 K trajectory. The NO_y content of T_{UCSE} + 1.5 K model run (blue line) is generally of a similar magnitude to that calculated from the isentropic models (red line), although with lower maxima. This is primarily due to the differences in the aerosol size distributions of the two runs. In the quasi-lagrangian model run, a higher proportion of the condensed phase NO_y is in particles with radii <0.1 µm than is the case for the combined result of the isentropic model runs. So, when we eliminate these particles, for comparison with the SIOUX data, the quasi-lagrangian test case is more severely affected. The difference is due to the temperature history of the quasi-lagrangian model run being warmer than that of the 445 K isentropic model run, which dominates the combined results at the observed maxima. However the difference between these model runs is small compared with their difference to the equilibrium calculations (grey line), and they are both better than the equilibrium calculations at capturing the magnitude of the SIOUX measurements.

In Fig. 8b we compare the backscatter coefficients from the MAS data (black line) and those calculated from our microphysical model (blue line). For these calculations we assume a refractive index of 1.43 for STS droplets (in line with the calculations of Luo et al., 1996). The peak values of the measured and modelled signals are of the same magnitude, and have a good temporal fit. However, throughout the rest of the mountain-wave event the modelled values are higher than those measured. This is because the stratospheric aerosol burden was lower than the standard values we used to initialise our model (see Sect. 5.2).

However we must note that our microphysical model does not simulate some features of the SIOUX and MAS measurements very well. Most notable is the uptake of NO_y predicted by the models and equilibrium calculations at $t \approx 0.5$ h, which is not seen in the measurements. Because of the detection limit of 0.3 ppbv NO_y for the SIOUX instrument (any signal features below this limit could be either real or artifact), we cannot be certain of the magnitude of the discrepancy between the models and measurements. However the absence of this feature within the measured mountain-wave PSC is supported by the MAS data (Fig. 8b). The most likely cause of these discrepancies are the simplifications and approximations which we have had to make in order to create the model trajectories. Because of the transient, non-stationary nature of the mountain waves on this day we are unable to get a better temporal fit to the observed data.

To remove the time-dependence of the data we have plotted it against $T-T_{NAT}$ (Fig. 9). T_{NAT} is calculated using the parameterisation of Hanson and Mauersberger (1988). For all data sets temperature and pressure are taken from the flight data. For data from our microphysical model (red and grey crosses) we calculate T_{NAT} using the fixed values of H_2O and HNO_3 given in Sect. 5.2. For the measured data (black crosses) we use the FISH and corrected SIOUX data to calculate T_{NAT}. Because of these different methods of calculating T_{NAT} the spread of $T-T_{NAT}$ values for the two data sets are slightly different. We note that the aerosol model seems to have been subjected to a slightly wider range of values of $T-T_{NAT}$, although some of this difference could be due to data gaps (calibration cycles) in the SIOUX measurements.

Comparing the measured (black crosses) and modelled (red crosses) particle NO_y data (Fig. 9a), we see a reasonable correlation between the two datasets at higher temperatures, although the modelled particle NO_y is about 1.5 ppbv below the measurement values at lower temperatures. We have previously noted that the aerosol size distributions during the quasi-lagrangian run are smaller than those from the isentropic model run which dominates at these low temperatures. Consequentually more NO_y is in the smaller particles, so adding the NO_y from these particles back into our results (cf. grey crosses in Fig. 9a) does go someway to reducing the disparity. This is a reasonable approach if we assume that the measured particles have a temperature history more similar to the isentropic trajectories, in which case they will be larger and so there will be less NO_y in particles with radii $<0.1\,\mu m$. The comparison of the measured (black crosses) and modelled (red crosses) backscatter coefficients shown in Fig. 9b confirms the good agreement between modelled and measured backscatter ratios, particularly as $T-T_{NAT}$ becomes more negative.

The results from the combined isentropic and $T_{UCSE}+1.5\,K$ microphysical model runs are, within our limitations, reasonable simulations of the SIOUX measurements. The mountain waves seen on the 8 February 2003 were not stable, so trajectories based on the aircraft data will not be perfect simulations of the actual isentropic trajectories. Additionally we have used mixing ratios based on averaged measurements within the mountain wave, which is again a simplification.

6.2. Heterogeneous chemical reactions

Using the microphysical model run, and the equilibrium calculations, along the $T_{UCSE}+1.5\,K$ trajectory we shall now examine the rates of the heterogeneous reactions during the model runs. These reactions depend on the particle surface area available, and so we shall begin by examining the relationship between the particle-phase NO_y contents shown in Fig. 8 and the aerosol surface areas generated by the two different methods.

The relationship between particle-phase NO_y content and surface area is partly dependent on the particle composition. During the $T_{UCSE}+1.5\,K$ model run our microphysical model shows a size-dependence of the changes in particle composition (Fig. 10a), which are not seen in the equilibrium calculations (Fig. 10b). We see that the composition of our microphysical model changes more slowly than that of the equilibrium code, as would be expected. In addition we note that the HNO_3 mass fractions in the equilibrium model reach 36–38%, while those of the microphysical model reach, at most, 22–24% – these compositional differences between the models are due mainly to the resistance to HNO_3 diffusion through the gas phase to the particle surfaces. As a result, the large differences in the NO_y content of the condensed phase seen in Fig. 8 are not as pronounced when looking at the differences in the total mass of the condensed phase between the two different methods. This can be seen in Fig. 11b, where we compare the total aerosol volumes from the equilibrium (red line) and dynamic (blue line) models. The differences between the two models are less than that seen in the NO_y data in Fig. 8. The difference is even less pronounced for the aerosol surface areas (Fig. 11a) because, unlike aerosol volume, particle surface areas are not linearly related to aerosol mass.

The production of Cl_2 and HOCl during the model run are shown in Fig. 12. The equilibrium code produces about 15% more Cl_2 than the microphysical model (99 pptv, compared with 85 pptv). This difference is principally due to the greater aerosol surface area seen in the equilibrium model (Fig. 11a). The HALOX instrument measured ClO_x ($ClO+2Cl_2O_2$) concentrations of around 300 pptv during this section of the flight; however, at this time, the solar zenith angle was about 110°. At such large zenith angles it is not straightforward to attempt to relate the measured ClO_x with the predictions of Cl_2 production from the model.

7. Conclusions

On the 8 February 2003, during the EuPLEx campaign, in-situ measurements of condensed-phase NO_y were made within mountain wave PSCs. Using dynamic microphysical, and equilibrium composition, models running along quasi-lagrangian trajectories – generated using flight data from the Geophysica, MM5 back-trajectories and MTP data – we have investigated the second, Northern, PSC event. We found that the particle-phase NO_y measurements could be best represented by interpolating the NO_y content calculated by our microphysical model along the isentropic trajectories created using the MTP data. However the NO_y content predicted by our microphysical model using the T_{UCSE} + 1.5 K trajectory is comparable to that calculated using the MTP trajectories. Equilibrium calculations along the T_{UCSE} + 1.5 K trajectory overpredict the particle-phase NO_y content in the first section of the mountain wave by up to a factor of 3, although they are better at capturing the shape of the later measurements. These simulations of the mountain wave event are limited by the short-lived and non-stationary nature of the mountain waves, as well as by our assumptions of the homogeneity of the mixing ratios of atmospheric gases. Bearing these caveats in mind, we conclude that the fit of the dynamic model to the measurements is reasonable, although we must be careful in making direct comparisons with the data. Within the simulated mountain wave our models produce 85–99 pptv Cl_2 (170–198 pptv Cl), which is a similar magnitude to the measured ClO_x mixing ratios. Unfortunately the solar zenith angle during this period is such that we cannot make any direct comparisons between modelled and measured ClO_x production; it would, however, be viable to make this comparison with measurements taken within similar mountain wave events occuring in sun light.

The differences in total aerosol mass between the two models are less than the differences in condensed-phase NO_y would suggest, because of the lower HNO_3 mass fractions of the dynamic model – which is due to a hysteresis effect in the evolution in composition of STS particles (Meilinger et al., 1995). The differences in the total aerosol surface areas are even smaller, because the mean particle radii of the dynamic model are smaller than those of the equilibrium model; consequently the equilibrium model only converts 15% more Cl_2 than the dynamic model. The differences in aerosol mass between the models, and so the differences in Cl_2 production, are very trajectory dependent. In this particular test case the average temperature within the mountain wave is 0.5–1.0 K above T_{STS} (the narrow ($\Delta T < 1$ K) temperature range at which the liquid aerosols change from a primarily binary sulphuric to a ternary composition). The drops in temperature below T_{STS} are too brief for condensation of large amounts of

HNO_3 to occur, so overall the dynamic model produces smaller aerosol masses than the equilibrium model. As the average temperature decreases so should the differences in mass between the models. Hence this 15% difference in Cl_2 production between the two models is not fixed; though more research is required to determine the range of ratios which could be expected for typical stratospheric mountain wave events.

The differences in Cl_2 production, due to surface area differences, between the two models are less than the reductions we could expect if we used parameterisations for Reactions (R1)–(R3) designed for ternary solutions. It is not clear from the few data points collated by Hanson (1998) whether the magnitude of the reduction in $ClONO_2$ uptake coefficients varies with the HNO_3 content of the solution. Because of the hysteresis effect – where the liquid PSC particles closely follow the composition curve of the binary sulphate solution upon cooling, and follow that of the binary nitric acid solution upon warming (see Meilinger et al., 1995) – such a composition dependence of Reactions (R1)–(R3) would lead to a greater decrease of the rates in the equilibrium model than in the dynamic model, possibly to the point of eliminating, or even reversing, the differences between the models. There is therefore a need for more laboratory studies of the heterogeneous reaction rates on ternary sulphuric/nitric solutions and more airbourne measurements of condensed NO_y simultaneous with measurements of gas-phase ClO_x.

Acknowledgements. Our thanks to F. Stroh and M. von Hobe for providing the HALOX data and for help with interpretation, M. Volk for providing the HAGAR data and for help with interpretation, and C. Schiller for providing the FISH data. Work performed at Lancaster University was supported by EU contract number EVK2-CT-2001-00119. Work performed at the Jet Propulsion Laboratory, California Institute of Technology, was carried out under a contract with the National Aeronautics and Space Administration. The ECMWF forecast and operational analyses were provided in the framework of the ECMWF special project "Influence of non-hydrostatic mountain waves on the stratosphere above Scandinavia" by one of the authors (A. Dörnbrack). We thank H. Wernli (University of Mainz, Germany) for his trajectory code. The mesoscale numerical simulations were performed on the NEC SX6 super computer of the German Climate Research Center (DKRZ) in Hamburg, Germany.

Title Page
Abstract | Introduction
Conclusions | References
Tables | Figures
◀▮ | ▶▮
◀ | ▶
Back | Close
Full Screen / Esc

Print Version

Interactive Discussion

EGU

References

Adriani, A., Cairo, F., Viterbini, M., Mandolini, S., Pulvirenti, L., and Di Donfrancesco, G.: Multiwavelength aerosol scatterometer for airborne experiments to study the optical properties of stratospheric aerosol, J. Atmos. Ocean. Tech., 16, 1329–1336, 1999. 9551, 9552

Brune, W. H., Anderson, J. G., and Chan, K. R.: Insitu Observations of ClO in the Antarctic – ER-2 Aircraft results from 54° S to 72° S Latitude, J. Geophys. Res., 94, 16 649–16 663, 1989. 9551

Carslaw, K. S., Luo, B. P., Clegg, S. L., Peter, T., Brimblecombe, P., and Crutzen, P. J.: Stratospheric Aerosol Growth and HNO$_3$ Gas Phase Depletion from Coupled HNO$_3$ and Water uptake by Liquid Particles, Geophys. Res. Lett., 21, 2479–2482, 1994. 9548

Carslaw, K. S., Luo, B., and Peter, T.: An analytic expression for the composition of aqueous HNO$_3$–H$_2$SO$_4$ stratospheric aerosols including gas phase removal of HNO$_3$, Geophys. Res. Lett., 22, 1877–1880, 1995. 9553

Carslaw, K. S., Wirth, M., Tsias, A., Luo, B. P., Dörnbrack, A., Leutbecher, M., Volkert, H., Renger, W., Bacmeister, J. T., and Peter, T.: Particle microphysics and chemistry in remotely observed mountain polar stratospheric clouds, J. Geophys. Res., 103, 5785–5796, 1998. 9549, 9550

Denning, R. F., Guidero, S. L., Parks, G. S., and Gary, B. L.: Instrument Description of the Airborne Microwave Temperature Profiler, J. Geophys. Res., 94, 16 757–16 765, 1989. 9551

Dörnbrack, A., Leutbecher, M., Volkert, H., and Wirth, M.: Mesoscale forecasts of stratospheric mountain waves, Meteorol. Appl., 5, 117–126, 1998. 9551

Dörnbrack, A., Leutbecher, M., Kivi, R., and Kyrö, E.: Mountain wave induced record low stratospheric temperatures above northern Scandinavia, Tellus, 51A, 951–963, 1999. 9550

Dörnbrack, A., Birner, T., Fix, A., Flentje, H., Meister, A., Schmid, H., Browell, E. V., and Mahoney, M. J.: Evidence for inertia gravity waves forming polar stratospheric clouds over Scandinavia, J. Geophys. Res., 107(D20), 8287, doi:10.1029/2001JD000452, 2002. 9550

Drdla, K.: Applications of a Model of Polar Stratospheric Clouds and Heterogeneous Chemistry, PhD thesis, University of California, Los Angeles, 1996. 9549

Drdla, K. and Schoeberl, M. R.: Microphysical modeling of the 1999–2000 Artic winter: 2. Chlorine activation and ozone depletion, J. Geophys. Res., 108(D5), 8319, doi:10.1029/2001JD001159, 2003. 9549

Fahey, D. W., Gao, R. S., Carslaw, K. S., Kettleborough, J., Popp, P. J., Northway, M. J., Holecek,

J. C., Ciciora, S. C., McLaughlin, R. J., Thompson, T. L., Winkler, R. H., Baumgardner, D. G., Gandrud, B., Wennberg, P. O., Dhaniyala, S., McKinney, K., Peter, T., Salawitch, R. J., Bui, T. P., Elkins, J. W., Webster, C. R., Atlas, E. L., Jost, H., Wilson, J. C., Herman, R. L., Kleinböhl, A., and von König, M.: The Detection of Large HNO_3-Containing Particles in the Winter Artic Stratosphere, Science, 291, 1026–1031, 2001. 9549

Hanson, D. and Mauersberger, K.: Laboratory Studies of the Nitrc Acid Trihydrate: Implications for the South Polar Stratosphere, Geophys. Res. Lett., 15, 855–858, 1988. 9548, 9559

Hanson, D. R.: Reaction of $ClONO_2$ with H_2O and HCl in Sulfuric Acid and $HNO_3/H_2SO_4/H_2O$ Mixtures, J. Phys. Chem. A, 102, 4794–4807, 1998. 9554, 9555, 9563

Jones, R. L., Soloman, S., McKenna, D. S., Poole, L. R., Brune, W. H., Toohey, D. W., Anderson, J. G., and Fahey, D. W.: The Polar Stratospheric Cloud Event of January 24, 1989: Part 2, Photochemistry, Geophys. Res. Lett., 17, 541–544, 1990. 9549

Krämer, M. and Afchine, A.: Sampling characteristics of inlets operated at low U/U_0 ratios: new insights from computational fluid dynamics (CFX) modeling, J. Aerosol Sci., 35, 683–694, 2004. 9552

Kühl, S., Dörnbrack, A., Wilms-Grabe, W., Sinnhuber, B.-M., Platt, U., and Wagner, T.: Observational evidence of rapid chlorine activation by mountain waves above northern Scandinavia, J. Geophys. Res., 109, D22309, doi:10.1029/2004JD004797, 2004. 9549

Lowe, D., MacKenzie, A. R., Nikiforakis, N., and Kettleborough, J.: A condensed-mass advection based model for the simulation of liquid polar stratospheric clouds, Atmos. Chem. Phys., 3, 29–38, 2003, SRef-ID: 1680-7324/acp/2003-3-29. 9550, 9554

Luo, B., Carslaw, K. S., Peter, T., and Clegg, S. L.: Vapour pressures of $H_2SO_4/HNO_3/HCl/HBr/H_2O$ solutions to low stratospheric temperatures, Geophys. Res. Let., 22, 247–250, 1995. 9554

Luo, B., Krieger, U. K., and Peter, T.: Densities and refractive indices of $H_2SO_4/HNO_3/H_2O$ solutions, Geophys. Res. Lett., 23, 3707–3710, 1996. 9558

Lutman, E. R., Pyle, J. A., Jones, R. L., Lary, D. L., MacKenzie, A. R., Kilbane-Dawe, I., Larsen, N., and Knudsen, B.: Trajectory model studies of ClO_x activation during the 1991/92 northern hemispheric winter, Geophys. Res. Lett., 21, 1419–1422, 1994. 9549

Mann, G. W., Davies, S., Carslaw, K. S., and Chipperfield, M. P.: Factors controlling Artic denitrification in cold winters of the 1990s, Atmos. Chem. Phys., 3, 403–416, 2003, SRef-ID: 1680-7324/acp/2003-3-403. 9549

Meilinger, S. K., Koop, T., Luo, B. P., Huthwelker, T., Carslaw, K. S., Krieger, U., Crutzen, P. J., and Peter, T.: Size-dependent Stratospheric Droplet Composition in lee wave Temperature Fluctuations and their potential role in PSC Freezing, Geophys. Res. Lett., 22, 3031–3034, 1995. 9562, 9563

Molina, M. J., Zhang, R., Wooldridge, P. J., McMahon, J. R., Kim, J. E., Chang, H. Y., and Beyer, K. D.: Physical Chemistry of the $H_2SO_4/HNO_3/H_2O$ System: Implications for Polar Stratopsheric Clouds, Science, 261, 1418–1423, 1993. 9548

Northway, M. J., Gao, R. S., Popp, P. J., Holecek, J. C., Fahey, D. W., Carslaw, K. S., Tolbert, M. A., Lait, L. R., Dhaniyala, S., Flagan, R. C., Wennberg, P. O., Mahoney, M. J., Herman, R. L., Toon, G. C., and Bui, T. P.: An analysis of large HNO_3-containing particles sampled in the Arctic stratosphere during the winter of 1999/2000, J. Geophys. Res., 107(D20), 8298, doi:10.1029/2001JD001079, 2002. 9549, 9551

Pilinis, C.: Derivation and Numerical Solution of the Species Mass Distribution Equations for Multicomponent Particulate Systems, Atmos. Environ., 24A, 1923–1928, 1990. 9554

Sander, S. P., Friedl, R. R., Ravishankara, A. R., Golden, D. M., Kolb, C. E., Kurylo, M. J., Huie, R. E., Orkin, V. L., Molina, M. J., Moortgat, G. K., and Finlayson-Pitts, B. J.: Chemical Kinetics and Photochemical Data for Use in Atmospheric Studies, Evaluation number 14, JPL Publication 02-25, Pasadena, 2003. 9549

Schauffler, S. M., Atlas, E. L., Donnelly, S. G., Andrews, A., Montzka, S. A., Elkins, J. W., Hurst, D. F., Romashkin, P. A., Dutton, G. S., and Stroud, V.: Chlorine budget and partitioning during the Stratospheric Aerosol and Gas Experiment (SAGE) III Ozone Loss and Validation Experiment (SOLVE), J. Geophys. Res., 108(D5), 4173, doi:10.1029/2001JD002040, 2003. 9556

Schmitt, J.: Aufbau und Erprobung eines in-situ-Mess-Systems am Höhenforschungsflugzeug M55-Geophysica, PhD thesis, ISSN 1434-8454, ISRN DLR-FB-2003-21, 2003. 9551

Schreiner, J., Voigt, C., Kohlmann, A., Arnold, F., Mauersberger, K., and Larsen, N.: Chemical Analysis of Polar Stratospheric Cloud Particles, Science, 283, 968–970, 1999. 9549

Sessler, J., Good, P., MacKenzie, A. R., and Pyle, J. A.: What role do type I polar stratospheric cloud and aerosol parameterizations play in modelled lower stratospheric chlorine activation and ozone loss?, J. Geophys. Res., 101, 28 817–28 835, 1996. 9549, 9550

Shi, Q., Jayne, J. T., Kolb, C. E., Worsnop, D. R., and Davidovits, P.: Kinetic model for reaction of $ClONO_2$ with H_2O and HCl and HOCl with HCl in sulfuric acid solutions, J. Geophys. Res., 106, 24 259–24 274, 2001. 9554, 9555

Stefanutti, L., MacKenzie, A. R., Santacesaria, V., Adriani, A., Balestri, S., Borrmann, S., Khattatov, V., Mazzinghi, P., Mitev, V., Rudakov, V., Schiller, C., Toci, G., Volk, C. M., Yushkov, V., Flentje, H., Kiemle, C., Redaelli, G., Carslaw, K. S., Noone, K., and Peter, T.: The APE-THESEO Tropical Campaign: An Overview, J. Atmos. Chem., 48, 1–33, 2004. 9551

Voigt, C., Schreiner, J., Kohlmann, A., Zink, P., Mauersberger, K., Larsen, N., Deshler, T., Kröger, C., Rosen, J., Adriani, A., Cairo, F., Donfrancesco, G. D., Viterbini, M., Ovarlez, J., Ovarlez, H., David, C., and Dörnbrack, A.: Nitric Acid Trihydrate (NAT) in Polar Stratospheric Clouds, Science, 290, 1756–1758, 2000a. 9548, 9549

Voigt, C., Tsias, A., Dörnbrack, A., Meilinger, S., Luo, B., Schreiner, J., Larsen, N., Mauersberger, K., and Peter, T.: Non-equilibrium compositions of liquid polar stratospheric clouds in gravity waves, Geophys. Res. Lett., 27, 3873–3876, 2000b. 9549

Voigt, C., Larsen, N., Deshler, T., Kröger, C., Schreiner, J., Mauersberger, K., Luo, B., Adriani, A., Cairo, F., Donfrancesco, G. D., Ovarlez, J., Dörnbrack, A., Knudsen, B., and Rosen, J.: In situ mountain-wave polar stratospheric cloud measurements: Implications for nitric acid trihydrate formation, J. Geophys. Res., 108(D5), 8331, doi:10.1029/2001JD001185, 2003. 9549

Voigt, C., Schlager, H., Luo, B. P., Dörnbrack, A., Roiger, A., Stock, P., Curtius, J., Vössing, H., Borrmann, S., Davies, S., Konopka, P., Schiller, C., Shur, G., and Peter, T.: Nitric acid trihydrate (NAT) formation at low NAT supersaturations, Atmos. Chem. Phys., 5, 1371–1380, 2005,
SRef-ID: 1680-7324/acp/2005-5-1371. 9551

von Hobe, M., Grooß, J.-U., Müller, R., and Stroh, F.: A Re-evaluation of the ClO/ClO Dimer Equilibrium Constant based on In-Situ Observations, Atmos. Chem. Phys., 5, 693–702, 2005,
SRef-ID: 1680-7324/acp/2005-5-693. 9551

Weisser, C., Mauersberger, K., Schreiner, J., Larsen, N., Cairo, F., Adriani, A., Ovarlez, J., and Deshler, T.: Composition analysis of liqiud particles in the Arctic stratopshere, Atmos. Chem. Phys. Discuss., 4, 2513–2531, 2004,
SRef-ID: 1680-7375/acpd/2004-4-2513. 9549

Wernli, H. and Davis, H. C.: A Lagrangian-based analysis of extratropical cyclones. 1. The method and some applications, Q. J. Roy. Meteor. Soc., 123, 467–489, 1997. 9555

WMO: Scientific Assessment of Ozone Depletion: 2002, Report 47, Global Ozone Research and Monitoring Project, Geneva, 2003. 9548

Worsnop, D. R., Fox, L. E., Zahniser, M. S., and Wofsy, S. C.: Vapor-Pressures of Solid Hydrates of Nitric-Acid – Implications for Polar Stratospheric Clouds, Science, 259, 71–74, 1993. 9548

Zhang, R., Wooldridge, P. J., and Molina, M. J.: Vapor Pressure Measurements for the $H_2SO_4/HNO_3/H_2O$ and $H_2SO_4/HCl/H_2O$ Systems: Incorporation of Stratospheric Acids into Background Sulfate Aerosols, J. Phys. Chem., 97, 8541–8548, 1993. 9548

Zöger, M., Afchine, A., Eicke, N., Gerhards, M. T., Klein, E., McKenna, D. S., Morschel, U., Schmidt, U., Tan, V., Tuitjer, F., Woyke, T., and Schiller, C.: Fast in situ stratospheric hygrometers: A new family of balloon-borne and airborne Lyman a photofragment fluorescence hygrometers, J. Geophys. Res., 104, 1807–1816, 1999. 9551

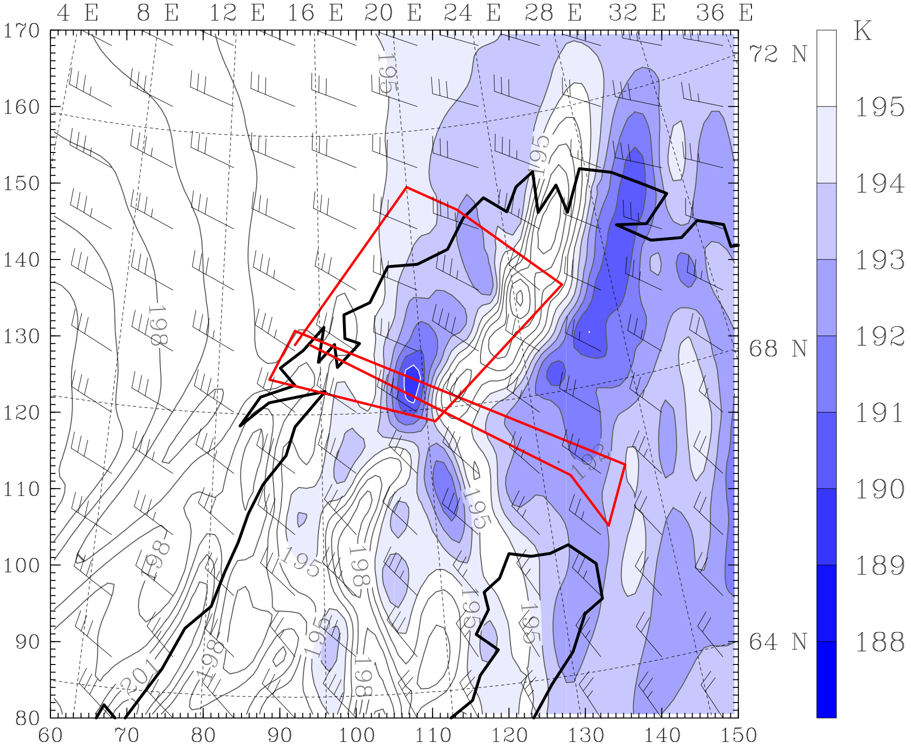

Fig. 1. Hindcast of air temperature at 50 mbar for 18:00 UTC, 8 February 2003 from the MM5 mesoscale model. The red line indicates the flight path of the Geophysica.

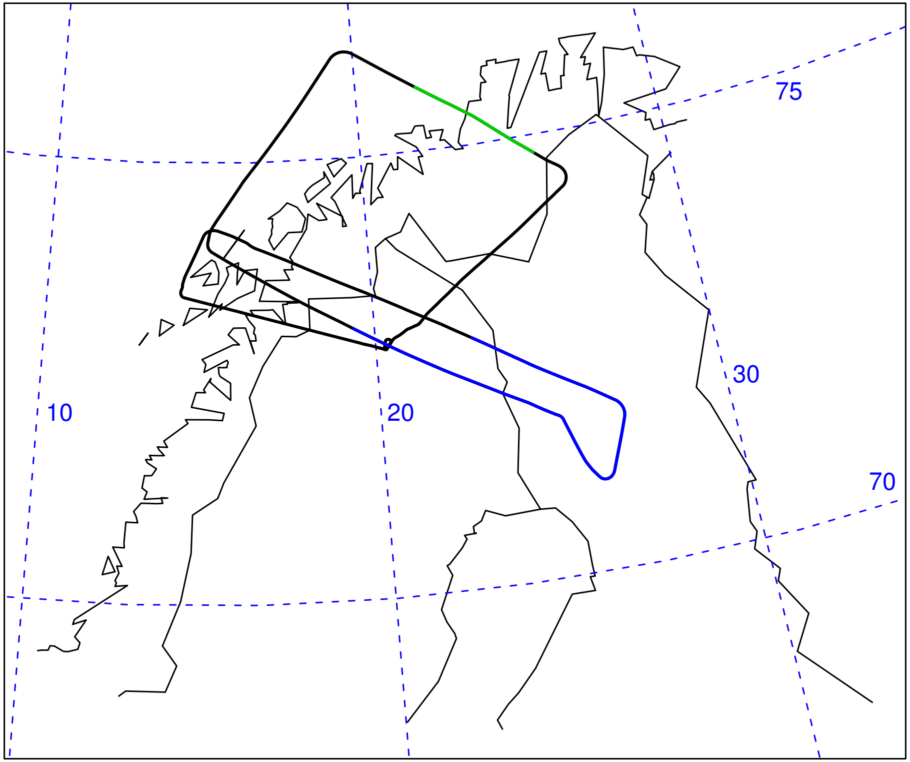

Fig. 2. Flight plan of the Geophysica aircraft on 8 February 2003. The green and blue sections roughly indicate where the aircraft passed through PSCs.

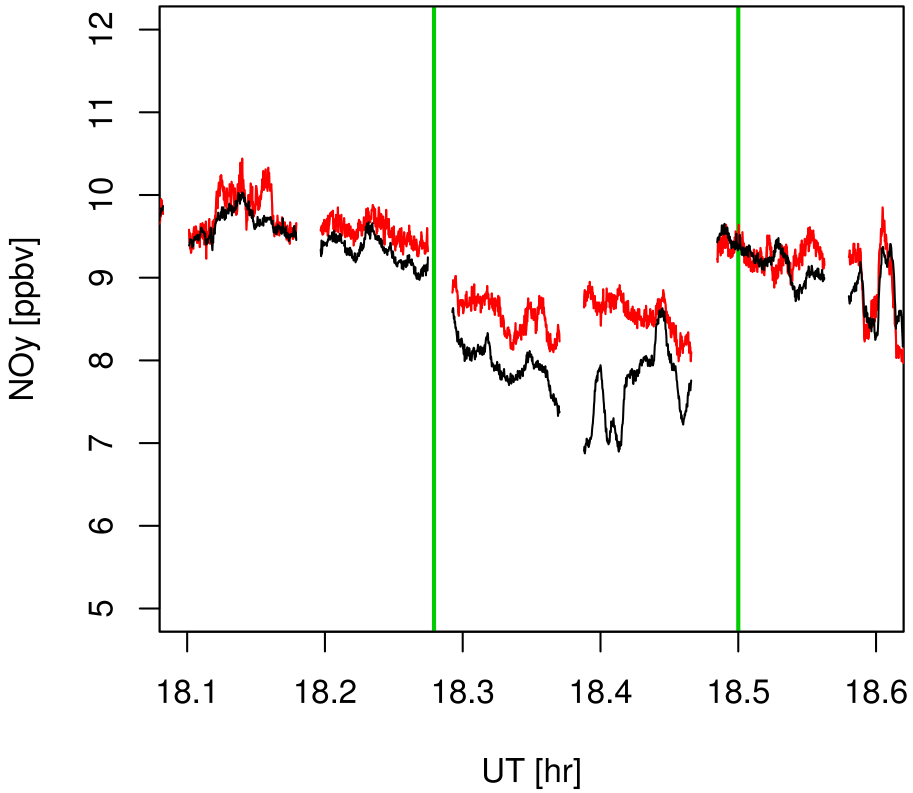

Fig. 3. Measured total (gas-phase plus 3.6 × particle-phase; red line) and gas-phase (black line) NO_y measured by the SIOUX instrument around the second PSC event on the flight on 8 February 2003. The green lines denote the edges of the region of PSCs marked by the green line in Fig. 2.

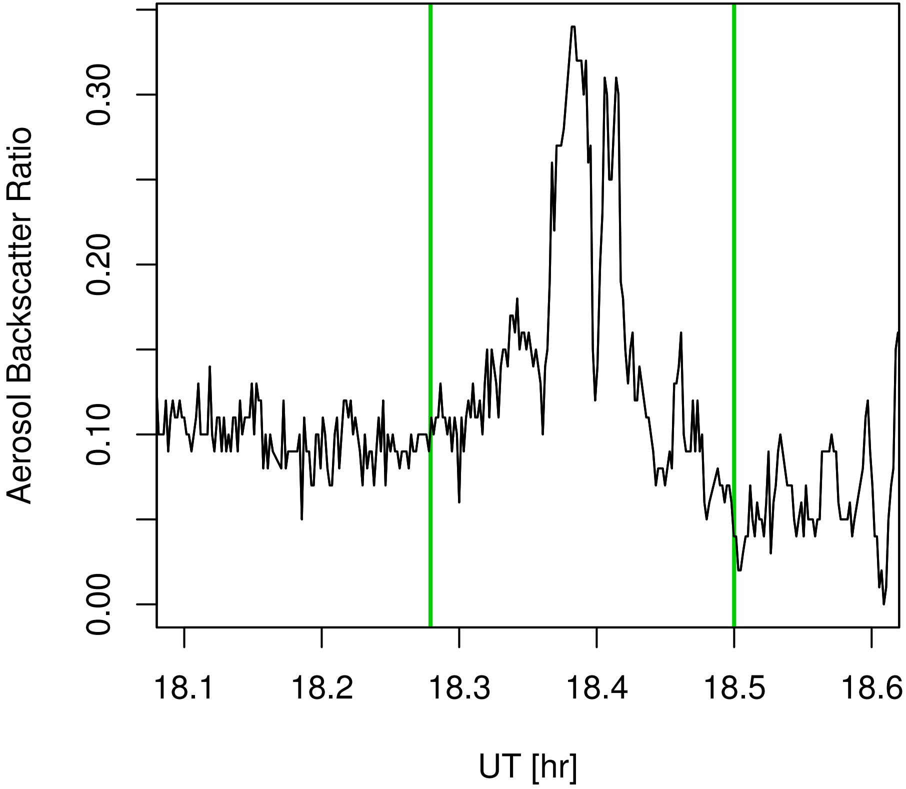

Fig. 4. Aerosol backscatter ratios measured by the MAS instrument. The green lines denote the edges of the region of PSCs marked by the green line in Fig. 2.

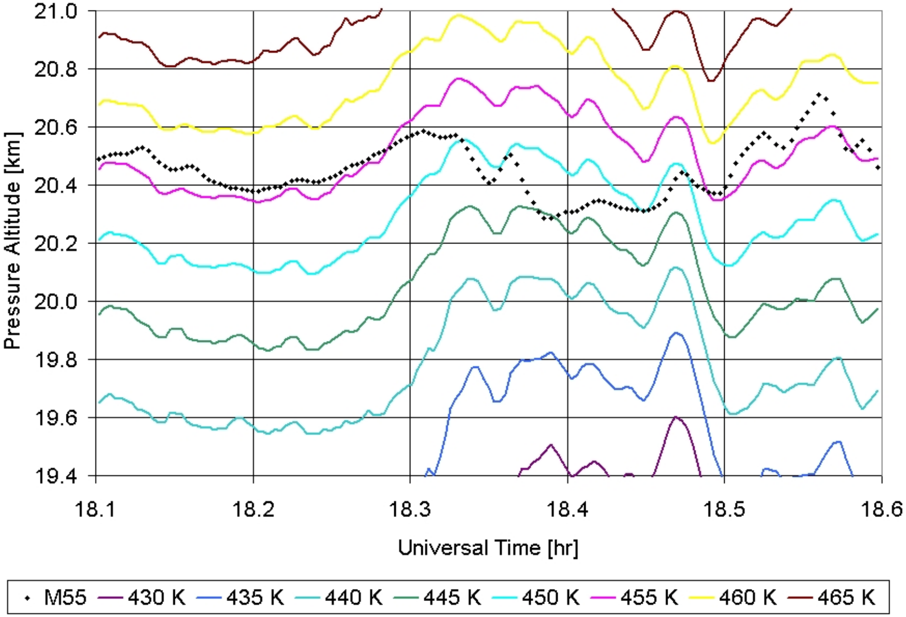

Fig. 5. Comparison of the pressure altitude of the Geophysica-M55 during the flight on the 8 February 2003 (black diamonds) with the pressure altitudes of isentropic surfaces (coloured solid lines) at 5 K intervals.

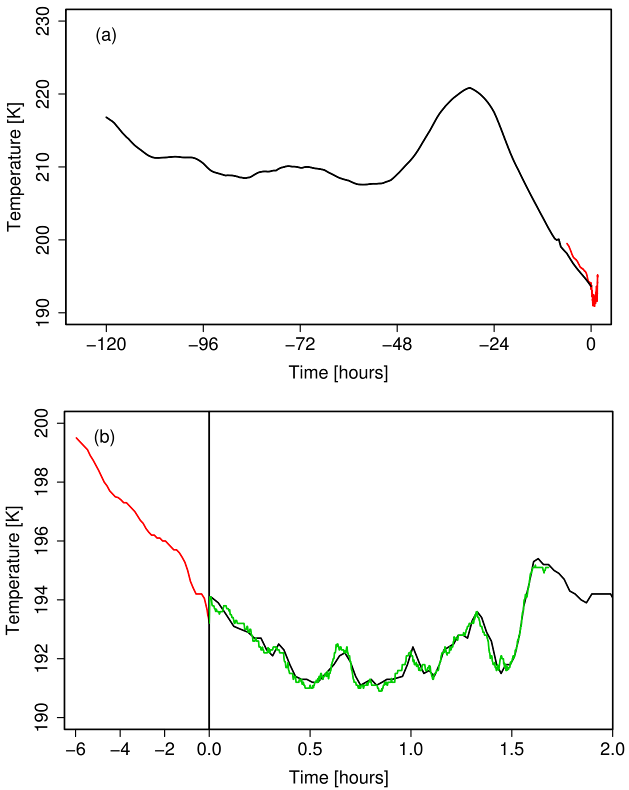

Fig. 6. **(a)** Temperature profile of the synoptic-scale (black line) back trajectory; the quasi-lagrangian trajectory used for the model runs is included for comparison (red line). **(b)** The quasi-lagrangian trajectory (combined red and green line) compared with the MTP temperature profile along the flight path (black line). The first (red) section of the trajectory is generated from a hindcast made using the MM5 model. The second (green) section is generated from the Geophysica flight data, the temperature is T_{UCSE} + 1.5 K. Maximum cooling rates during the composite T_{UCSE} + 1.5 K are 0.04 Ks^{-1} over 5 s and 0.004 Ks^{-1} over 900 s.

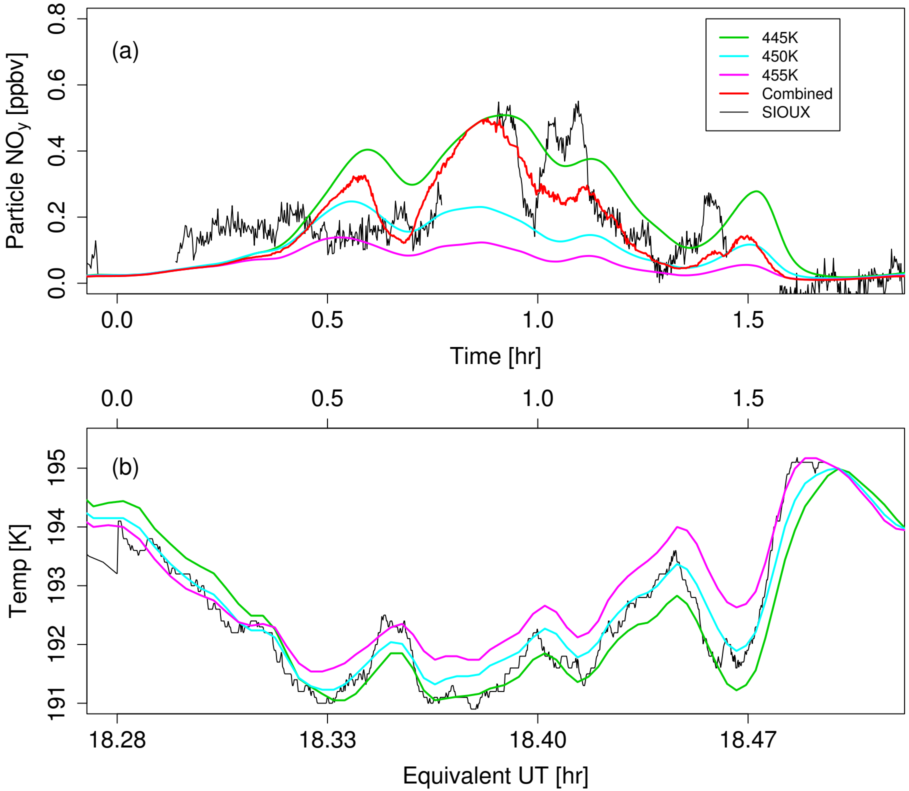

Fig. 7. **(a)** NO$_y$ content of the condensed phase for our non-equilibrium model along the isentropes measured by the MTP instrument (green, light blue and purple lines, as identified in the legend), combined NO$_y$ content along the aircraft trajectory from the isentrope data (red line), and measured by the SIOUX instrument (black line). **(b)** The temperature profiles along the isentropic trajectories (green, cyan and purple lines as identified in the legend in Fig. 7a), as well as the T_{UCSE} + 1.5 K temperature profile. Note that, because of the method we use to expand the timescale, the relationship between model time and the equivalent UT is not linear.

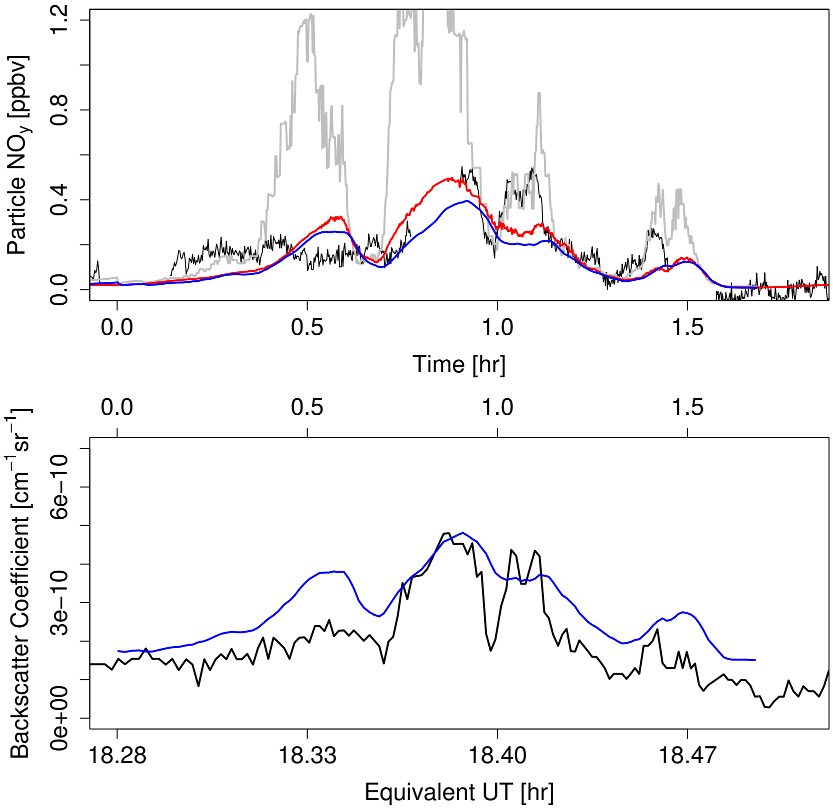

Fig. 8. **(a)** NO_y content of the condensed phase for our microphysical model (blue line) and equilibrium calculations (grey line) along the T_{UCSE} + 1.5 K trajectory, compared with those measured by the SIOUX instrument (black line) and calculated along the T_{UCSE} + 1.5 K trajectory using the data from the isentropic trajectories shown in Fig. 7 (red line). **(b)** Backscatter coefficients calculated from the MAS data (black line) and our microphysical model (blue line). The uncertainty of the MAS data varies around $5.5\times10^{-12}\,cm^{-1}sr^{-1}$; around 3% of the signal within the mountain wave.

Title Page
Abstract
Introduction
Conclusions
References
Tables
Figures
◀◀
▶▶
◀
▶
Back
Close
Full Screen / Esc

Print Version

Interactive Discussion

EGU

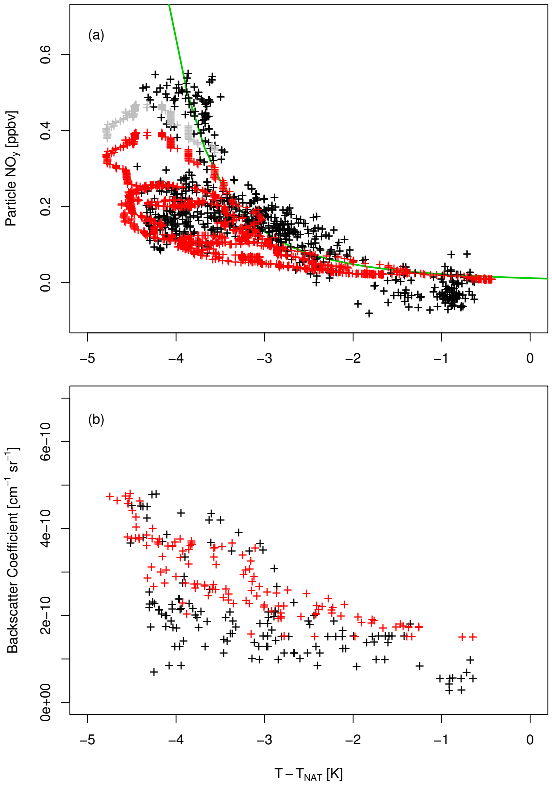

Fig. 9. **(a)** NO_y content of the condensed phase, within the mountain wave, for our microphysical model (red crosses) and the SIOUX data (black crosses) against $T-T_{NAT}$. The green line represents the equilibrium composition of STS at the mixing ratios mentioned in Sect. 5.2 and at a pressure of 50 mbar. The grey crosses represent the NO_y content of the condensed phase of our microphysical model without removing the NO_y contained in particles with radii <0.1 µm **(b)** Aerosol backscatter coefficients within the mountain wave for our microphysical model (red crosses) and the MAS data (black crosses) against $T-T_{NAT}$.

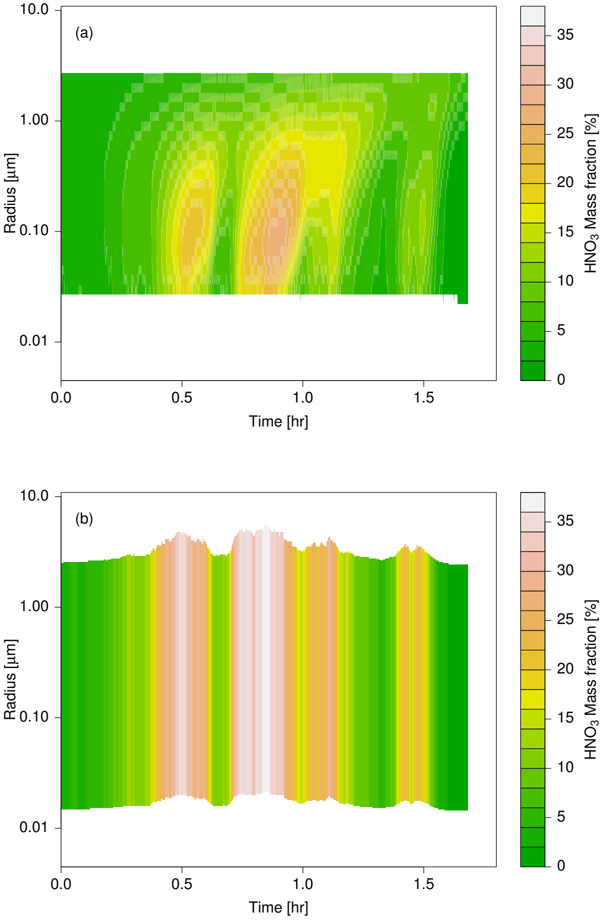

Fig. 10. The changes in HNO$_3$ mass fraction across the particle size range during the T_{UCSE} + 1.5 K model run shown in Fig. 8 for **(a)** our microphysical model and **(b)** the equilibrium model.

Title Page
Abstract Introduction
Conclusions References
Tables Figures
◀▮ ▶▮
◀ ▶
Back Close
Full Screen / Esc
Print Version
Interactive Discussion
EGU

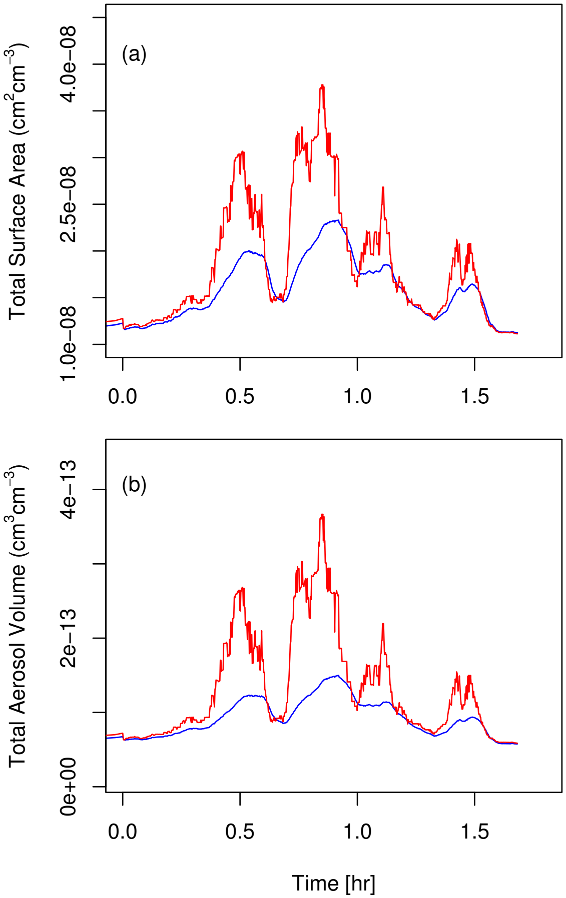

Fig. 11. Comparisons of the total aerosol **(a)** surface area and **(b)** volume produced from the equilibrium (red lines) and dynamic (blue lines) models in the T_{UCSE} + 1.5 K test case.

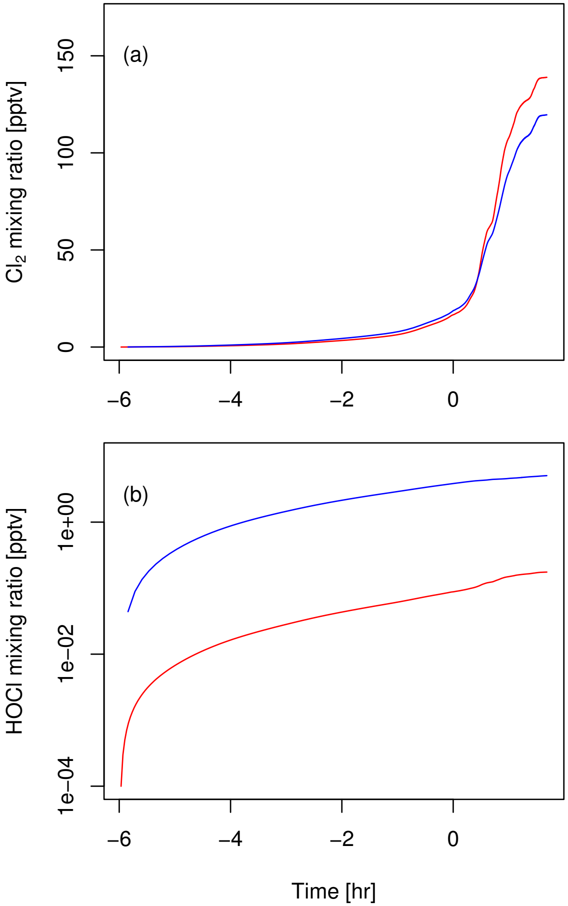

Fig. 12. Production of **(a)** Cl_2 and **(b)** HOCl during the T_{UCSE} + 1.5 K model runs shown in Fig. 8. The blue line indicates the output from our microphysical model, the red line that from the equilibrium code.